Published online 6 October 2021

Nucleic Acids Research, 2021, Vol. 49, No. 19 ***10835–10850***
https://doi.org/10.1093/nar/gkab888

Binding of DNA origami to lipids: maximizing yield and switching via strand displacement

Jasleen Kaur Daljit Singh[1,2,3,†], Esther Darley[4,†], Pietro Ridone[4], James P. Gaston[4], Ali Abbas[2,3], Shelley F.J. Wickham[1,3,5,*] and Matthew A.B. Baker[4,6,*]

[1]School of Chemistry, The University of Sydney, Sydney, New South Wales, Australia, [2]School of Chemical and Biomolecular Engineering, The University of Sydney, Sydney, New South Wales, Australia, [3]The University of Sydney Nano Institute, The University of Sydney, Sydney, New South Wales, Australia, [4]School of Biotechnology and Biomolecular Sciences, University of New South Wales, Sydney, Australia, [5]School of Physics, The University of Sydney, Sydney, New South Wales, Australia and [6]CSIRO Synthetic Biology Future Science Platform, Brisbane, Australia

Received July 23, 2021; Revised September 1, 2021; Editorial Decision September 15, 2021; Accepted September 20, 2021

ABSTRACT

Liposomes are widely used as synthetic analogues of cell membranes and for drug delivery. Lipid-binding DNA nanostructures can modify the shape, porosity and reactivity of liposomes, mediated by cholesterol modifications. DNA nanostructures can also be designed to switch conformations by DNA strand displacement. However, the optimal conditions to facilitate stable, high-yield DNA–lipid binding while allowing controlled switching by strand displacement are not known. Here, we characterized the effect of cholesterol arrangement, DNA structure, buffer and lipid composition on DNA–lipid binding and strand displacement. We observed that binding was inhibited below pH 4, and above 200 mM NaCl or 40 mM $MgCl_2$, was independent of lipid type, and increased with membrane cholesterol content. For simple motifs, binding yield was slightly higher for double-stranded DNA than single-stranded DNA. For larger DNA origami tiles, four to eight cholesterol modifications were optimal, while edge positions and longer spacers increased yield of lipid binding. Strand displacement achieved controlled removal of DNA tiles from membranes, but was inhibited by overhang domains, which are used to prevent cholesterol aggregation. These findings provide design guidelines for integrating strand displacement switching with lipid-binding DNA nanostructures. This paves the way for achieving dynamic control of membrane morphology, enabling broader applications in nanomedicine and biophysics.

INTRODUCTION

DNA nanotechnology is an approach to designing and building nanostructures that self-assemble via DNA hybridization (1). Since its development (2), a large number of 2D and 3D DNA nanostructures have been reported (3,4). The precise addressability of DNA nanostructures allows for patterned functionalization with nanoparticles (5,6), proteins (7,8) and hydrophobic groups (9,10), resulting in applications in nanofabrication (11,12), biosensing (13,14) and membrane targeting (9,15). Alongside this, in the field of DNA computing, increasingly complex computational circuits have been realized with DNA molecules in solution, driven by the process of toehold-mediated DNA strand displacement (16,17). The combination of structural and dynamic DNA nanotechnology has resulted in environment-sensing mechanisms that allow DNA nanostructures to change state in response to external triggers (18).

Modification of DNA with hydrophobic chemical groups, such as cholesterol (9,19,20), alkyl chains (21), tocopherol (15), polypropylene oxide (22) and porphyrins (10,23), has been used to enable lipid membrane binding (24). Cholesterol-modified DNA nanostructures have been used to functionalize liposome surfaces (25), induce membrane curvature and tubulation (26,27), and form membrane-spanning nanopores that facilitate current flow (9). For example, DNA nanopores can have dimensions that exceed those of natural protein pores (28), and can incorporate mechanisms that regulate ion flow in response to external stimuli, termed gating (20,29).

A range of lipid-interacting cholesterol-modified DNA nanostructures have been realized to date, but systematic studies of the lipid binding efficiency of cholesterol-modified DNA nanostructures are still incomplete (Figure

*To whom correspondence should be addressed. Email: matthew.baker@unsw.edu.au
Correspondence may also be addressed to Shelley F.J. Wickham. Email: shelley.wickham@sydney.edu.au
†The authors wish it to be known that, in their opinion, the first two authors should be regarded as Joint First Authors.

1A). The diverse range of design parameters over which to optimize includes DNA nanostructure shape (1D, 2D, 3D) and size (20–10 000 bp); hydrophobic modification type, number, position, tether geometry and strand displacement reversibility; membrane composition and cholesterol content; buffer components (Na^+, Mg^{2+}); and liposome size and curvature (100 nm to 40 μm). To date, only limited subsets of this parameter space have been explored systematically (Figure 1A).

The number and position of cholesterol groups on DNA nanostructures have been observed to affect nanostructure docking and diffusion in lipid bilayers (9,30–32). The effect of cholesterol number and position on membrane binding has been investigated most systemically for a large (∼7000 bp, 110 nm × 16 nm × 8 nm) 3D rod-like '20 helix-bundle' nanostructure (30,31), assembled from a long scaffold strand using the DNA origami folding method (33). It was found that more cholesterol groups increased binding, up to a maximum of five tested (30). Cholesterol position was found to be more important than number, with edge-placed groups having the greatest increase in binding. Diffusion on bilayers decreased with the number of corner cholesterol groups. The effect of position and number has also been compared for three DNA origami shapes: a wireframe sphere (80 nm diameter), a long rod (400 nm × 5 nm) and a flat 2D rectangle (90 nm × 70 nm) (34). In this case, membrane binding was not achieved by hydrophobic modification of nanostructures, but instead via DNA hybridization between nanostructure single-stranded DNA (ssDNA) 'overhangs' and modified ssDNA 'anchors' on cell membranes. Similarly, binding increased with overhang number (up to 28) but position was found to be more important, with edge-placed groups providing the largest increase in binding for all shapes. The overall binding yield was determined by comparing nanostructure interaction between cells with and without anchors, and for the three shapes the yield was in the order of rod, 2D tile and 3D sphere. Small (<500 bp, 7 nm × 7 nm × 7 nm) 3D cube DNA nanostructures, assembled from short synthetic DNA strands ('unscaffolded') (32), have also been tested with up to eight cholesterols. In this case, the mobile fraction of DNA nanostructures on the membrane also decreased with increasing cholesterols, and when cholesterols were on both sides compared to one side.

However, there still remains a gap in the systemic study of cholesterol-modified nanostructures with higher numbers (>8) and different shapes. Many reported membrane-interacting nanostructures incorporate much larger numbers of hydrophobic groups, up to 18–26 (9,15,28,35). The large numbers of hydrophobic groups are thought to be necessary to overcome the substantial energy penalties associated with the insertion of membrane-spanning DNA nanopores (36), but have been found to promote aggregation of the modified DNA nanostructures and reduce yield (15,37). The shape and size of DNA origami nanostructures have also been shown to affect cellular uptake (38,39) and membrane binding (30). In particular, the original 2D DNA origami tile (33) is of interest for membrane binding as its modular staple arrangement and large surface area to volume ratio make it ideal as a molecular pegboard for functionalization with other molecules, and its flexible geometry (40) gives it the potential to take on the shape and curvature of a membrane.

The effect of the tether length and orientation of hydrophobic groups has also been shown to be important for both binding yield and aggregation of DNA nanostructures. Spacers enhance binding, with a larger increase observed for double-stranded DNA (dsDNA) spacers compared to ssDNA, and this effect is greater for designs with fewer cholesterols or centrally positioned cholesterols (31). Unfortunately, spacers also increase the cholesterol-mediated aggregation of DNA nanostructures (41). Adding an ssDNA 'overhang' proximal to the cholesterol group has been shown to reduce such aggregation (41). However, the effect of this protective overhang on membrane binding is yet to be quantitatively evaluated. Cholesterol-induced aggregation has also been minimized by labelling cell membranes directly with ssDNA–cholesterol anchors that capture DNA nanostructures from solution (34), but this approach is not suitable for *in vivo* applications. Thus, tether optimization requires a balance of application type, aggregation and binding yield, which requires more comprehensive systematic data.

Reversibility in membrane binding allows for complex regulatory mechanisms to be achieved in many biological systems. For instance, amphitropic proteins such as the RAS family (42), hisactophilin (43) and Src kinase (44) utilize reversible membrane binding for regulation of catalytic function and signalling complexes (45,46). While these systems are present extensively in biology, such reversibility is lacking in DNA–lipid systems. In one study, reversible membrane binding of a wireframe DNA prism nanostructure was achieved using strand displacement (47). The results show that it was necessary to decorate the invader strand with cholesterols for successful displacement of the DNA prism (47). Cation-dependent reversible membrane binding of DNA duplexes has also been demonstrated (48). However, the reversibility of membrane binding is yet to be demonstrated with solid DNA origami nanostructures. Reversible membrane binding could be useful in DNA-assisted liposome formation and purification. Currently, nucleases are standardly used to separate DNA nanostructures from lipid membranes upon liposome formation and purification (49,50). However, this method may not be suitable for downstream applications that are nuclease sensitive. Reversibility in membrane binding could facilitate nuclease-free removal of DNA nanostructures from liposomes in such instances. DNA toehold design plays an important role in the strand displacement of DNA nanostructures (51,52), and evidence is emerging that common hydrophobic DNA modifications such as fluorophores can significantly affect strand displacement (53).

Finally, monovalent and divalent cations are necessary buffer components for assembly and stability of DNA duplexes and nanostructures (54,55), yet are also known to affect the physical characteristics of membrane bilayers (56,57) and may affect the binding activity of cholesterol-modified DNA (58). Lipid composition plays a further role. For example, for 3D rod nanostructures, using DOPC:DOPS (9:1) decreased membrane binding compared to using DOPC alone (31). For short (<100 bp) DNA oligomers binding to liposomes, ideal ionic con-

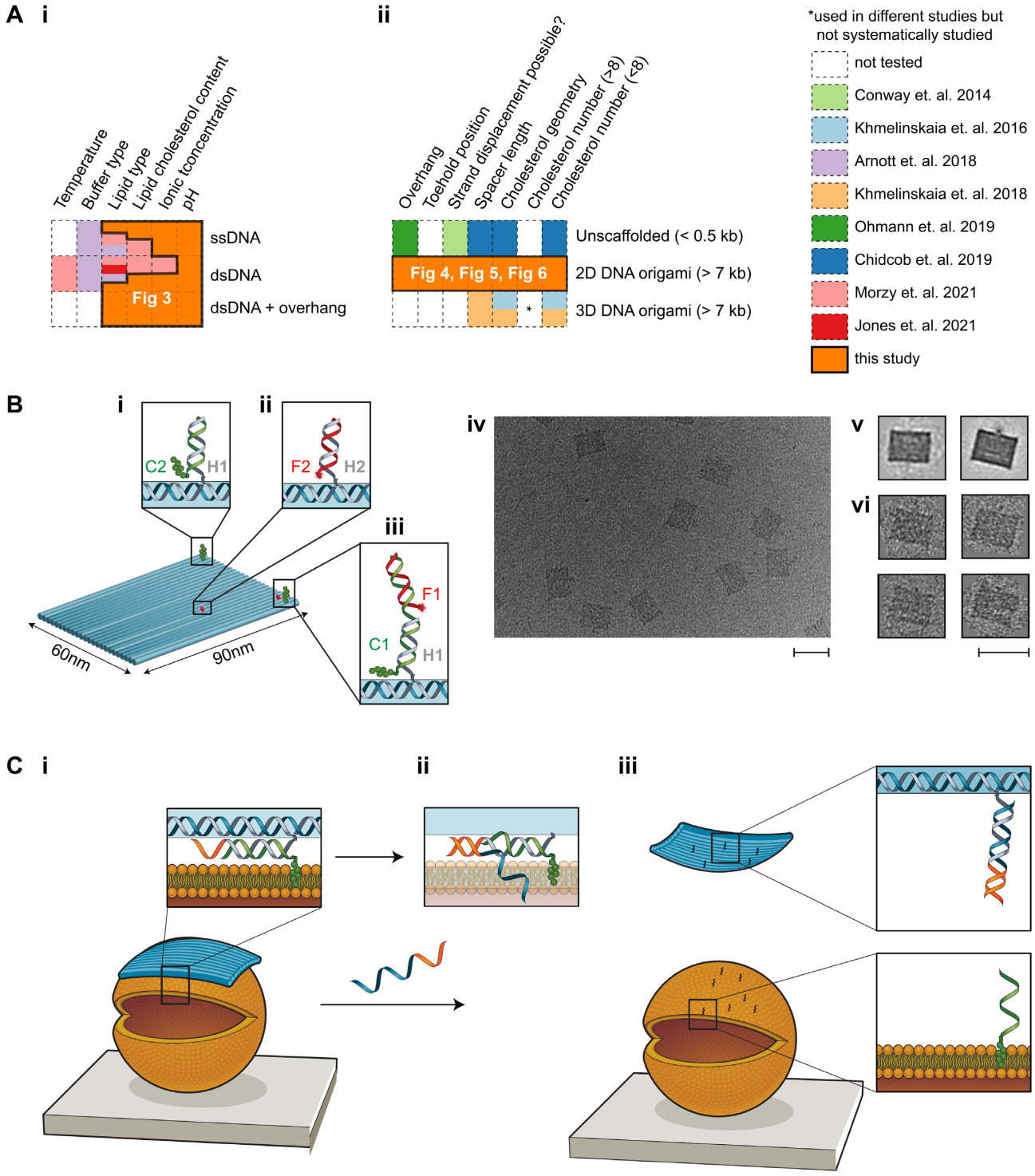

Figure 1. Overview of this work. **(A)** Matrix table highlighting previous studies on membrane binding of cholesterol-modified **(i)** DNA strands and **(ii)** DNA nanostructures, and the gaps filled by our study. **(B)** Schematic of the DNA origami tile. **(i)** Cholesterol (green blobs)-labelled strand C2 hybridizes with handle H1 on the tile (scaffold strand is shown in blue in insets). **(ii)** Cy5-labelled strand F2 hybridizes with handle H2 on the tile. **(iii)** Cholesterol-labelled strand C1 hybridizes with handle H1 on the tile, as well as Cy5-labelled strand F1. **(iv)** Transmission electron microscopy (TEM) image of the DNA origami tile (no cholesterol). Scale bar: 100 nm. **(v)** Averaged TEM image of tile obtained using RELION. Two different averaged structures were obtained, with minor differences resulting from staining. **(vi)** TEM images of single tiles. Scale bar: 100 nm. **(C) (i)** Schematic of the binding of the tile (blue) to a liposome (orange). Inset: Schematic showing the DNA strand (grey) extending from the tile, which is hybridized to a cholesterol strand (green) and has a toehold (orange) for strand displacement. Cholesterol is shown embedded in the lipid bilayer. **(ii)** Upon addition of a displacement strand (blue–orange), branch migration initiates. **(iii)** When strand displacement is complete, the tile is released from the liposome and the cholesterol–DNA remains attached.

ditions have been shown to vary lipid type (48,58). For PE/PC, greater binding was found at 0.3 M KCl, while for PE/PG greater binding was seen in phosphate-buffered saline, and for both lipid types binding was greater in KCl for dsDNA in comparison with ssDNA (58). The type of hydrophobic modification has also been shown to affect membrane binding. Cholesterol-modified dsDNA demonstrated greater membrane binding when compared with alkyl phosphorothioate-modified dsDNA, on liposomes made from POPC and POPC:DPPC (1:1) (59). Membrane cholesterol content also affected binding with greatest binding for a POPC:cholesterol ratio of 1:1 (versus no cholesterol or a ratio of 1:2).

Membrane binding has also been observed in the absence of cholesterol labelling, with DNA duplexes binding to gel-phase DPPC liposomes in the presence of divalent cations such as magnesium and calcium (48). No membrane binding was observed in the presence of monovalent cations alone or in liquid-phase membranes (achieved with an increase in temperature or an increase of cholesterol content in the membrane from 0% to 25% or the use of POPC liposomes). Liquid-phase POPC membrane binding was possible with the use of cholesterol-labelled ssDNA and dsDNA, with binding increasing as the concentration of magnesium ions increased from 0 to 4 mM. Thus, achieving the best match between DNA structure and lipid/buffer conditions remains a challenge.

In this work, we fill gaps in our understanding of how DNA–membrane binding is affected by the parameters discussed above. We present a systematic optimization of the number, position and geometry of cholesterol attachment sites on a 2D rectangular DNA nanostructure, as well as buffer and lipid composition, to improve the efficiency of membrane binding of DNA strands. We have quantified the binding of cholesterol-modified DNA strands to synthetic liposomes using fluorescence microscopy, including the effects of pH, ion concentration, membrane composition and cholesterol content. We investigated three types of DNA motif: ssDNA, dsDNA and a duplex with a short ssDNA 'overhang' proximal to the cholesterol group, recently shown to reduce aggregation during nanostructure assembly (41). Next, we investigated the membrane binding efficiency of a cholesterol-modified 2D DNA origami nanostructure using fluorescence microscopy and a high-throughput gel shift assay. The effects of cholesterol number, configuration and spacer distance between the DNA nanostructure and cholesterol were tested. We then optimized strategies for achieving reversible membrane binding by controlled removal of membrane-bound DNA nanostructures using toehold-mediated strand displacement.

MATERIALS AND METHODS

Preparation of buffers and solutions

Liposomes and DNA stocks were diluted in liposome buffer (210 mM D-sorbitol, 5 mM Tris–HCl, pH 7.5) containing NaCl (12.5–400 mM) and $MgCl_2$ (0–80 mM) as required. For NaCl-dependent experiments, the $MgCl_2$ concentration was kept at 10 mM, while for $MgCl_2$-dependent experiments, the NaCl concentration was kept constant at 100 mM. For pH-dependent experiments, a modified liposome buffer (210 mM D-sorbitol, 100 mM NaCl) was used, with pH adjusted to 2, 4, 6, 7, 8 and 10 ± 0.2 with 200 mM NaOH or HCl.

Design and assembly of ssDNA and dsDNA

DNA strands used for lipid-binding experiments were 23 nt in length, and used as ssDNA, dsDNA or dsDNA with a 5′ 6-nt single-stranded 'overhang' (dsDNA-6nt) (Supplementary Data). DNA sequences were designed using NUPACK design software (60) to prevent unwanted secondary structures. A previously published 6-nt overhang sequence was added to the 5′ end of oligos (41). Oligos were purchased modified at the 3′ end with a tetraethylene glycol cholesterol moiety (TEG-cholesterol) and/or at the 5′ end with Alexa647, Cy5 or Cy3 fluorophores.

DNA stocks (100 μM, 1000×) were prepared using Milli-Q water and stored at 4°C. For dsDNA assembly, non-fluorescent complementary strands were added in a 3-fold excess to fluorescent-modified strands and annealed (90°C for 5 min, and then 90–15°C at a rate of −5°C/min) at 10 μM final concentration in duplex buffer (100 mM NaCl, 5 mM Tris–HCl, pH 7.5). Annealed dsDNAs were stored at 4°C. DNA was diluted in extrusion buffer (210 mM sorbitol, 100 mM NaCl, 5 mM Tris–HCl, pH 7.5) to 100 nM for lipid-binding experiments. Excess strands were not removed in order to ensure the overall concentration of fluorescent strands remained constant at 100 nM for all samples in all experiments.

Preparation of liposomes

Liposomes were produced with two lipid mixtures: (1) DOPE/DOPC liposomes (49.9% 1,2-dioleoyl-*sn*-glycero-3-phosphoethanolamine, 49.9% 1,2-dioleoyl-*sn*-glycero-3-phosphocholine) and (2) DPhPC liposomes (99.8% 1,2-diphytanoyl-*sn*-glycero-3-phosphocholine) (Supplementary Tables S1 and S2). Both lipid mixtures were doped with 0.1% PE-rhodamine (1,2-dioleoyl-*sn*-glycero-3-phosphoethanolamine-*N*-lissamine rhodamine B sulfonyl) for fluorescence imaging and 0.1% PE-biotin (1,2-dioleoyl-*sn*-glycero-3-phosphoethanolamine-*N*-biotinyl) for surface tethering. All percentages indicate weight to weight ratios. Liposomes with cholesterol were prepared by replacing either DPhPC (lipid type 2) or equal parts of DOPE and DOPC (lipid type 1) with cholesterol. All lipids stocks were dissolved in chloroform at 10 mg/ml and stored at −20°C.

Extruded liposomes, termed small unilamellar vesicles (SUVs), were produced using a Mini-Extruder kit using 100 nm membrane pore size (Avanti Polar Lipids Inc., USA) in matched buffer conditions to the final test conditions (i.e. osmolarity and buffer composition matched across the bilayer) and according to the manufacturer's protocol (Supplementary Methods). Liposomes were then diluted 100-fold to 0.1 mg/ml final lipid concentration in the same buffer in which liposomes were formed prior to experiments (i.e. for 100 mM NaCl, pH 7.5, experiments, extrusion buffer was 210 mM sorbitol, 100 mM NaCl and 5 mM Tris–HCl, pH 7.5).

Giant unilamellar liposomes (GUVs) were prepared by electroformation using the Vesicle Prep Pro machine (Nan-

ion Technologies GmbH, Germany) using the default protocol as described previously (61) (Supplementary Methods). GUVs in electroformation solution (210 mM sorbitol, pH 7.5) were diluted 1:1 in buffer of 210 mM sorbitol, 80 mM NaCl and 10 mM Tris–HCl, giving a final external solution of 210 mM sorbitol, 40 mM NaCl and 5 mM Tris–HCl. Liposome dissolution was tested by titration of increasing concentration of the detergent Polysorbate 20 (Supplementary Figure S1).

TIRF microscopy of DNA binding to extruded SUVs

Surfaces for imaging were prepared using tunnel slides and BSA–biotin/avidin conjugation chemistry as described previously (62,63). Briefly, first BSA–biotin was flowed into the tunnel slide to coat and both block the surface and provide sparse, available biotin groups on the surface. Then, streptavidin was flowed into the tunnel slide in excess to conjugate to the available biotin groups on the surface. The unbound streptavidin was then washed out and the biotinylated liposomes were flowed in, whereupon the liposome could tether to the available streptavidin binding sites, conjugating the liposome to the surface via BSA–biotin–avidin linkage.

DNA motifs were flowed into the slide upon SUV tethering on the slide. For DNA–SUV binding experiments, ssDNA or dsDNA strands were flowed into the slide at 100 nM. For experiments with DNA origami tiles, the tiles were flowed in at 10 nM. In both cases, DNA strands or DNA tiles were incubated on the slide for 1 h prior to imaging.

Surface-tethered SUVs and DNA were imaged using a Zeiss Elyra PALM/SIM Microscope in total internal reflection fluorescence (TIRF) mode with a 63×/1.4 Oil Iris M27 oil immersion objective (Carl Zeiss AG, Germany) and Andor iXon 897 EMCCD camera (Oxford Instruments, UK). Two-channel fluorescence images were collected for rhodamine liposomes (excitation/emission filters 561/570–650 plus 750 nm long pass) and fluorophore-tagged DNA (excitation/emission filters 642/655 nm long pass). Exposure times were 100 ms (lipid) and 33 ms (DNA), and images were averaged over two subsequent acquisitions.

Confocal fluorescence microscopy of DNA binding to electroformed GUVs

For DNA–GUV binding, 5 nM of DNA strands were used. DNA binding on GUVs was imaged using a Leica TCS SP8 DLS confocal microscope with HC PL APO CS2 63× oil immersion objective lens, acousto-optical beam splitter and programmable crystal-based beam splitter (Leica Microsystems GmbH, Germany). Two-channel images with rhodamine liposomes (excitation/emission 561/569-611 nm) and Alexa647-DNA (excitation/emission 640/690-734 nm) were imaged with a line averaging of two.

Quantification of DNA–liposome binding from microscope images

A custom macro script was developed using FIJI in ImageJ (64) to quantify the colocalization of DNA and liposomes, based on the Manders overlap coefficient (65). An intensity threshold was chosen as two standard deviations above the mean pixel intensity in the liposome channel over all images from a single experimental condition. This threshold was then used to create a binary mask for assigning pixels as either liposome or non-liposome, and thus identify liposomes from the background (Supplementary Methods, Supplementary Figures S2 and S3). This method was found to show no bias or correlation with liposome area (percentage coverage), in comparison with Pearson's correlation, which did show such bias (Supplementary Figures S4 and S5). Our measurements are ratiometric between liposome-bound and background dye, and we also confirmed that underlying raw fluorescence intensity was not affected by salt concentration (Supplementary Figure S6).

The mean pixel intensities of the DNA channel for the liposome and background areas were then compared, and used to calculate a colocalization ratio, C_R, via

$$C_R = F_{DNA,lipid} / F_{DNA,background},$$

where C_R is the reported colocalization ratio, $F_{DNA,lipid}$ is the mean pixel intensity of the fluorescent DNA in the liposome region of the DNA channel and $F_{DNA,background}$ is the mean pixel intensity of the fluorescent DNA in the background region of the DNA channel (Supplementary Figure S3).

Assembly of DNA origami nanostructures

To decorate the DNA tile with cholesterols, 21-nt ssDNA handles (H1) were designed for hybridization with complementary cholesterol-TEG-modified DNA strands (C1 or C2). To quantify binding of cholesterol–DNA to the tile, strand C1 was designed with a second binding domain for hybridization of Cy5 fluorophore-labelled DNA (F1) (Figure 1B-iii). For membrane-binding experiments, strand C2, without the second domain, was used (Figure 1B-i). To label the tile with fluorophores for microscopy, separate 21-nt ssDNA handles (H2) were extended from the surface of the tile for hybridization with Cy5-labelled ssDNA F2 (Figure 1B-ii). In this design for microscopy, the number of fluorophores on the tile is independent of the number of cholesterols. The positions of H1 on the tile are given in Figure 4A and Supplementary Figure S9, and the positions of H2 are given in Supplementary Figure S10.

DNA sequences for DNA origami tile structure (33) were obtained using the Picasso software (66). The tile was folded using 10 nM of M13mp18 ssDNA scaffold and 10× excess (100 nM) of DNA staple strands in folding buffer (5 mM Tris, 1 mM EDTA, 12 mM $MgCl_2$, pH 8.0) and annealed over 3 h (80°C for 15 min, and then 60–4°C in 56 steps at 3 min 12 s/step). Cholesterol-TEG-modified DNA strands (C1 or C2) were added to staple pools prior to annealing at 2× excess relative to staple concentration (e.g. for 4C tile, C1/C2 = 100 nM × 4 × 2 = 800 nM). For fluorophore attachment to cholesterol strands, F1 strand was added at 2× excess to the amount of C1 (e.g. for 4C tile, F1 = 800 nM × 2 = 1600 nM). For fluorescence labelling of tile, 2000 nM of F2 strand was added as there are 10 H2 handles on the tile (so, F2 = 100 nM × 10 × 2 = 2000 nM). All staples, plain and modified, were annealed in one pot. All sequences used are supplied in the Supplementary Data.

Purification of DNA origami by agarose gel electrophoresis

For analysis of membrane binding by gel, DNA origami tiles were purified by agarose gel electrophoresis (AGE) (67). Samples were loaded on 2% agarose gels and run for 2.5 h at 60 V at room temperature (RT). Gel and running buffer used was 0.5× TBE buffer (45 mM Tris–boric acid, 45 mM Tris base, 1 mM EDTA, pH 8) with 11 mM $MgCl_2$, and gels were pre-stained with SYBR Safe stain. Gels were viewed under an LED Blue Light Transilluminator (Fisher Biotec) and the bands corresponding to the DNA origami tile were cut. The cut bands were transferred into Freeze 'N Squeeze DNA Gel Extraction spin columns (Bio-Rad), crushed and extracted by centrifugation at 18 000 × *g* and 4°C for 10 min. The concentration of the recovered solution was determined using a Nanodrop (Thermo Fisher Scientific) to measure absorption at 260 nm. DNA origami tiles were stored at 4°C.

Purification of DNA origami by PEG precipitation

DNA origami tiles were purified by PEG precipitation (68) for all microscopy experiments. The folded DNA origami tile sample was mixed at 1:1 ratio with PEG buffer [15% PEG 8000 (w/v), 5 mM Tris, 1 mM EDTA and 505 mM NaCl] and incubated at 4°C for 30 min. The solution was centrifuged at 15 000 × *g* and 4°C for 30 min. The supernatant was removed using a pipette and discarded. The remaining pellet was air dried and then dissolved in the buffer (5 mM Tris–HCl, 40 mM NaCl, 10 mM $MgCl_2$).

Gel shift assay to quantify membrane binding of DNA origami

Agarose gel shift assays were conducted to determine the extent of membrane binding of DNA origami nanostructures (58,69). Ten microlitres of 2.5 nM gel purified DNA origami tile was incubated with 5 μl of extruded SUVs (diluted 20× in 5 mM Tris–HCl, 40 mM NaCl, 10 mM $MgCl_2$ upon extrusion) for 30 min at RT. Ten microlitres of sample was loaded onto a 2% agarose gel prepared in 0.5× TBE buffer (45 mM Tris–boric acid, 45 mM Tris base, 1 mM EDTA, pH 8.0) supplemented with 11 mM $MgCl_2$. The gel was run at 60 V for 2.5 h at 20°C, and imaged using Chemidoc MP Imager (Bio-Rad). Images were obtained in the Cy5 channel and analysed using the Bio-Rad Image Lab software.

This assay allowed for the separation of unbound tiles from membrane-bound tiles (Figure 4C). For each tile design, two gel lanes were run: (1) tiles incubated with liposomes (sample lane) and (2) tiles only, no liposomes (control lane). The intensity of the tile band was compared between the sample and control lanes to quantify the extent of membrane binding. The ratio of the intensity of the tile band in the sample lane (+ liposomes, red box in Figure 4C-i) to the intensity of the tile band in the control lane (− liposomes, black box in Figure 4C-i) was determined to calculate the percentage of bound tiles:

$$T = \left(1 - \frac{B}{U}\right) \times 100\%,$$

where T is the estimated percentage of tiles that are bound to the membrane, B is the intensity of the tile band in the lane with liposomes and U is the intensity of the tile band in the lane without liposomes. To account for experimental variation in loading of DNA into the gel, at least two repeats of each gel were conducted.

TEM of DNA origami

Fifteen microlitres of 1 nM (in 5 mM Tris, 1 mM EDTA, 12 mM $MgCl_2$, pH 8.0) purified DNA origami tile sample was placed onto a parafilm, and a plasma-treated carbon-coated TEM grid (Ted Pella EM grids from ProScitech) was placed onto the sample and left for 1 min for the sample to adsorb onto the grid. A 2 μl droplet of 2% uranyl acetate solution was placed onto a fresh parafilm and the grid was then quickly tapped onto the droplet and immediately tapped onto a filter paper to remove excess stain. This staining protocol was repeated three times. TEM imaging was performed using the JEOL JEM-1400 microscope, 120 kV. TEM micrographs of the DNA tiles were averaged using RELION (70) (Supplementary Figure S11).

RESULTS

DNA origami nanostructure design and assembly

The 2D rectangle DNA origami tile (Figure 1B) was chosen due to its ease of assembly and wide use in the field of DNA nanotechnology (37,66,71). The tile consists of 24 parallel DNA helices folded using the M-13 scaffold and has dimensions of 60 nm × 90 nm × 2 nm. Successful assembly of the tile and incorporation of fluorophore-modified staple strands was verified using AGE (Supplementary Figure S8) and TEM (Figure 1B-iv and Supplementary Figure S11).

Imaging of DNA–liposome binding

Sample homogeneity for SUVs was characterized using light scattering (Supplementary Figure S7) and then colocalization of fluorescent DNA to fluorescent liposomes was measured using TIRF microscopy. Colocalization was observed only when DNA oligomers were modified with cholesterol (Figure 2C). In contrast, DNA without cholesterol was distributed evenly throughout the image independently of the position of liposomes (Figure 2A). Similarly, in confocal images of GUVs, plain DNA did not colocalize (Figure 2B), whereas cholesterol-modified DNA colocalized with the GUVs (Figure 2D).

Effect of buffer and lipid composition on DNA–liposome binding

The effect of DNA origami buffer components on the binding of cholesterol–DNA to SUVs was quantified. The colocalization ratios (C_R) of cholesterol-modified ssDNA, dsDNA and dsDNA-6nt were measured for varying [NaCl], [$MgCl_2$] and pH, for 1:1 DOPE/DOPC liposomes and DPhPC liposomes, and compared to plain DNA controls (Figure 3).

DNA that was evenly distributed throughout a slide independently of liposome location would be expected to produce a C_R value of 1.0. Membrane-bound DNA, on the other hand, would be expected to produce a C_R of >1.0,

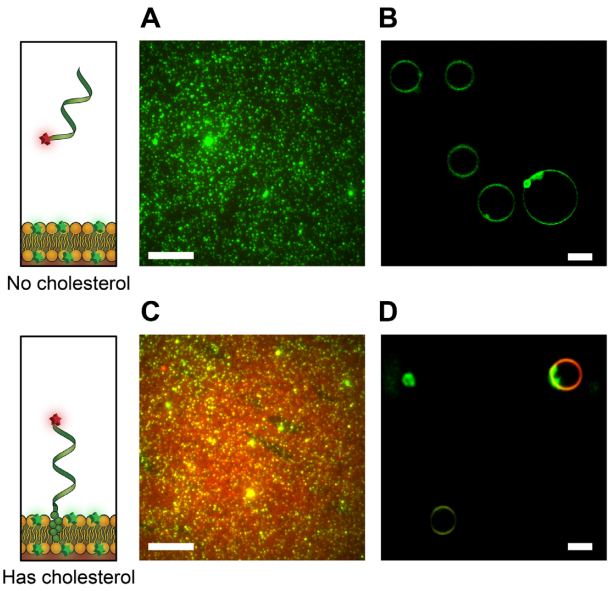

Figure 2. Binding of cholesterolated DNA to liposomes. **(A)** Merged two-colour TIRF images of ssDNA Alexa647–DNA oligomer (red) at 100 nM concentration and PE-rhodamine-labelled DOPE/DOPC SUVs (green). C_R for image in (A) is 1.0332. **(B)** Confocal image of ssDNA Alexa647–DNA oligomer (red) at 5 nM and rhodamine-labelled DOPE/DOPC GUVs (green). **(C)** Merged two-colour TIRF images of ssDNA Alexa647–DNA–cholesterol oligomer (red) at 100 nM concentration and PE-rhodamine-labelled DOPE/DOPC SUVs (green). C_R for image in (C) is 1.9436. **(D)** Confocal image of ssDNA Alexa647–DNA–cholesterol oligomer (red) at 5 nM and rhodamine-labelled DOPE/DOPC GUVs (green). For TIRF images (A, C, 16 bit), brightness is scaled with min = 1500 au and max = 7000 au. For GUVs, image scaled (B, D, 8 bit) with min = 30 and max = 255. For all images, buffer conditions are 210 mM sorbitol and 5 mM Tris–HCl, pH 7.5; for (A, C), NaCl 25 mM; for (B, D), NaCl 50 mM. All scale bars: 10 μm.

as the concentration of DNA on liposomes is expected to be higher than the concentration on the background. For DNA without cholesterol, the C_R was measured as 1.01 ± 0.03 for all NaCl, pH, $MgCl_2$ and lipid conditions tested, indicating low non-specific interaction between the DNA and liposomes. In each case, we compared colocalization ratio of cholesterolated dye–DNA with dye-only DNA demonstrating that the non-specific background binding from the dye was negligible. In comparison, the colocalization ratio for cholesterol–DNA configurations when pooled across all conditions was significantly higher than that without cholesterol ($C_R = 1.70 \pm 0.36$, $P < 0.05$; excluding measurements for cholesterolated DNA at pH 2.0 measurements yields $C_R = 1.73 \pm 0.34$, $P < 0.05$). This confirmed that specific binding of cholesterol–DNA to liposomes was observed.

For all three configurations of cholesterol–DNA (ssDNA, dsDNA, dsNDA-6nt) on both DOPE/DOPC liposomes and DPhPC liposomes, a significant decrease was observed in C_R between 12.5 and 400 mM NaCl and between 0 and 80 mM $MgCl_2$. Linear regression analysis for all three configurations on both liposome compositions showed a trend of decreasing colocalization scores with increasing concentrations of NaCl and $MgCl_2$ (95% CI of gradient <0).

DNA–liposome binding was tested for pH values between 2 and 10 and the C_R of cholesterol–DNA was observed to decrease in highly acidic conditions. At pH 2, the C_R of all three configurations of cholesterol–DNA with both DOPE/DOPC liposomes (Figure 3E) and DPhPC liposomes (Figure 3F) decreased to a level similar to the non-cholesterol control strands, and was significantly less than that at all other pH values ($P < 0.05$). This indicates that solutions of pH 2 inhibit membrane binding.

Effect of DNA configuration on lipid binding

Significant differences were observed in mean C_R for the different DNA configurations. In both DOPE/DOPC liposomes and DPhPC liposomes, we found dsDNA to colocalize more than ssDNA, in the order $C_{R(dsDNA)} \approx C_{R(dsDNA\text{-}6nt)} > C_{R(ssDNA)}$. When compared to dsDNA, the addition of the 6-nt overhang in dsDNA-6nt was observed to cause a modest but significant decrease in binding to DPhPC liposomes, but no significant decrease in binding to DOPE/DOPC liposomes (Figure 3I and J).

Effect of membrane cholesterol content on DNA–lipid binding

Cholesterol content was increased between 0% and 40% by mass for both lipid compositions. For DOPE/DOPC liposomes, C_R of all three configurations of cholesterol–DNA showed a significant increase between 0% and 40% cholesterol ($P < 0.05$). Linear regression analysis showed a trend of increasing C_R across the observed range of membrane cholesterol content (95% CI of gradient >0) (Figure 3G).

For DPhPC liposomes, C_R of cholesterol-tagged DNA increased to a maximum at 10–20% membrane cholesterol, and then decreased with further increasing cholesterol. All three configurations of cholesterol–DNA showed both a significant increase in C_R between 0% and 20% ($P < 0.05$) and a significant decrease in C_R between 20% and 40% ($P < 0.05$) (Figure 3H).

Effect of number of cholesterols on membrane binding of DNA origami tile

First, the correct assembly of cholesterol–DNA (C1) (Figure 1B) to the DNA tile was verified using AGE (Supplementary Figure S12) and TEM (Supplementary Figure S13). The tile was folded with either 0, 1, 2, 4, 8 or 16 cholesterol (0C, 1C, 4C-LS, 8C, 16C) moieties (Figure 4A and Supplementary Figure S9). Cy5 fluorophore-labelled strand F1 is designed to hybridize to the tile only in the presence of cholesterol–DNA C1. A comparison was made of Cy5 intensity of the DNA tile band (normalized to SYBR Safe-stained DNA channel) for samples with different numbers of cholesterol–DNA sites. The normalized Cy5 intensity was found to increase with increasing cholesterol number (Supplementary Figure S12). This successfully confirmed that more cholesterol–DNA strands attached to the tile as the number of handles (H1) increased from 0 to 16.

The effect of cholesterol number on membrane binding was then observed by AGE and fluorescence microscopy (TIRF). In AGE, the DNA tiles were observed to migrate

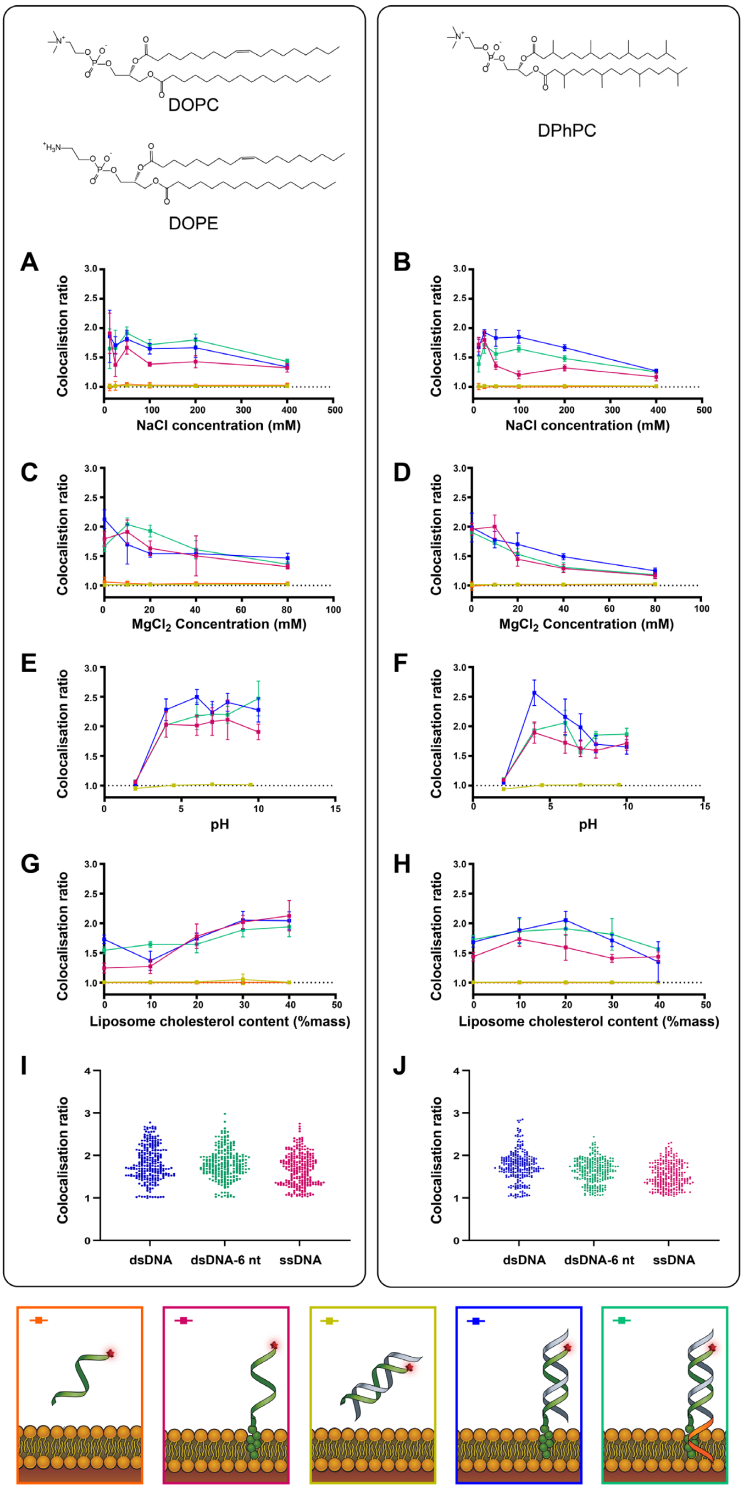

Figure 3. The effect of NaCl, $MgCl_2$, pH and membrane cholesterol on DNA–liposome colocalization in SUVs. Colocalization ratios and standard deviations are shown for Alexa647-labelled cholesterol-tagged ssDNA (pink), cholesterol-tagged dsDNA (blue) and cholesterol-tagged dsDNA-6nt (green) as well as dsDNA with no cholesterol tag (yellow) and ssDNA with no cholesterol tag (orange) and rhodamine-labelled DOPE/DOPC liposomes (left column, **A**, **C**, **E**, **G**) and DPhPC liposomes (right column, **B**, **D**, **F**, **H**). Solution conditions tested included (**A**, **B**) extrusion buffer [NaCl] containing 12.5, 25, 50, 100, 200 and 400 mM NaCl, (**C**, **D**) extrusion buffer [$MgCl_2$] containing 0, 10, 20, 40 and 80 mM $MgCl_2$, and (**E**, **F**) extrusion buffer [pH] adjusted to pH values of 2, 4, 6, 7, 8 and 10. (**G**, **H**) The effect of lipid cholesterol content was tested by forming liposomes from DOPE/DOPC and DPhPC lipid stocks containing 0%, 10%, 20%, 30% or 40% cholesterol. (**I**, **J**) Distribution of C_R values for each cholesterol-tagged DNA configuration across all conditions ($n = 264$; DOPE/DOPC: dsDNA $= 1.82 \pm 0.41$; dsDNA-6nt $= 1.80 \pm 0.35$; ssDNA $= 1.68 \pm 0.37$; DPhPC: dsDNA $= 1.74 \pm 0.36$, dsDNA-6nt $= 1.63 \pm 0.28$, ssDNA $= 1.53 \pm 0.29$, all mean $\pm$ SD). For both lipid types and with or without overhang, ssDNA versus dsDNA showed a significant difference in mean (Wilcoxon rank sum test, $P < 0.05$). For DPhPC only, there was a significant difference in mean, albeit smaller than the associated error measurement ($\Delta C_R = 0.10 \pm 0.46$) between dsDNA and dsDNA-6nt (Wilcoxon rank sum test, $P < 0.05$).

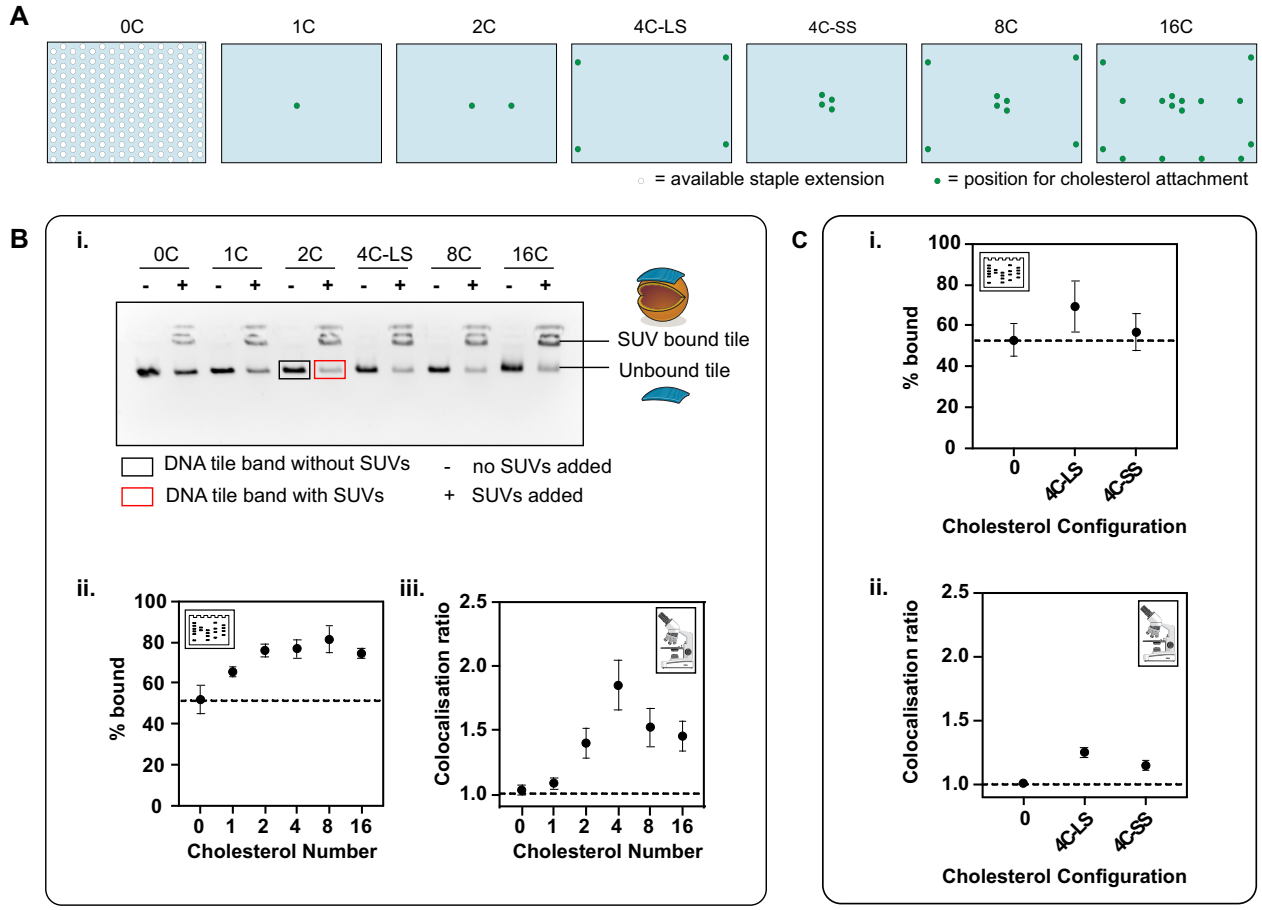

Figure 4. Effect of number and configuration of cholesterols on membrane binding. **(A)** The different attachment points available on the DNA origami tile (light blue rectangle) for staple extensions (white circle) and the points selected for staple extension of handles H1 (green circle) for cholesterol attachment. **(B)** The effect of cholesterol number on membrane binding. **(i)** Gel image. **(ii)** Percentage bound from the gel analysis calculated from ratio of integrated band intensity in the presence of liposomes (red box) to the integrated band intensity in the absence of liposomes (black box). **(iii)** Colocalization ratios from microscopy. **(C)** The effect of cholesterol configuration on membrane binding. **(i)** Percentage bound obtained from gel analysis. **(ii)** Colocalization ratios from microscopy.

through the gel matrix, while the liposomes remained in the wells (Supplementary Figure S14), in agreement with literature results using this technique (58). The percentage of tiles bound to the membrane was 52 ± 5% for tile-0C, indicating significant non-specific membrane binding even in the absence of cholesterols (Figure 4B-ii and Supplementary Figure S15). A significant increase in percentage of tiles bound was observed from tile-0C to tile-8C ($P < 0.01$). Maximum binding of tiles to liposomes was observed for tile-8C at 81 ± 5%.

For microscopy experiments, the maximum colocalization of tile and liposomes was observed on tiles with four cholesterol groups ($C_R = 1.85 \pm 0.20$) (Figure 4B-iii). A significant increase in C_R was observed between $n = 0$ and $n = 4$ cholesterol groups ($P < 0.05$), with a trend of increasing colocalization as the number of cholesterol groups was increased within this range (linear regression between $n = 0$ and $n = 4$: 95% CI of gradient >0). For the control with no cholesterol, $C_R = 1$, indicating similar density of DNA in the background and on the liposome. Linear regression analysis across $n = 4$, $n = 8$ and $n = 16$ showed a decreasing trend as the number of cholesterol groups was increased (95% CI of gradient <0); however, there was no significant difference in the means from pairwise testing.

Effect of cholesterol geometry on membrane binding of DNA origami tile

We next investigated the effect of cholesterol–DNA geometry on membrane binding. Two different geometries were compared: large square (4C-LS) and small square (4C-SS), as shown in Figure 4A-i. In the LS configuration, four cholesterol anchors were positioned along the edge of the tile. The separation between the handles in the 4C-LS configuration is 80 nm along the long edge and 45 nm along the short edge of the tile. In the 4C-SS configuration, four cholesterol anchors were positioned at the centre of the tile, with a separation of 5 nm between the handles. The percentage of tiles bound to the membrane was 69 ± 12% and 57 ± 9% for 4C-LS and 4C-SS configurations, respectively, using the gel shift assay (Figure 4C-i and Supplementary Figure S16). The percentage of tiles bound non-specifically in the no-cholesterol sample was 53 ± 8%, similar to results discussed in the previous section. The differences in mem-

brane binding between the no-cholesterol control, the 4C-LS and the 4C-SS geometries were found not to be statistically significant.

For the microscopy assay, C_R values of 1.25 ± 0.04 and 1.15 ± 0.03 were obtained for the 4C-LS and 4C-SS configurations, respectively (*t*-test $P < 0.05$, Figure 4C-ii). These C_R values are lower than those previously observed for the tile with four cholesterols shown in Figure 4B-iii, but we note that the C_R values vary with different SUV preparation batches but are consistent within a single SUV preparation.

The extent of cholesterol attachment for the 4C-LS and 4C-SS geometries was measured by AGE (method as above, Supplementary Figure S17) to determine whether the difference observed in membrane binding between these samples was due to different levels of cholesterol attachment to the tile. No differences in cholesterol attachment were observed for the two tile configurations, suggesting that the differences observed in lipid binding were due to the different geometrical arrangements of the cholesterols on the tile.

Effect of spacer length between cholesterol and tile on membrane binding

Next, the effect of the spacer length between the cholesterol and the tile on membrane binding was observed. Seven different spacer designs were tested: Dt1.4, Dt6.1, Dt8.1, Pt8.1, Pt8.5, Pt13.2 and Dt15.2, where the number gives the distance between the cholesterols and the tile; e.g. Dt15.2 represents an estimated spacing of 15.2 nm. The initial (Dt or Pt) refers to the positioning of the toehold relative to the cholesterol, either distal to the cholesterol (Dt) or proximal to the cholesterol (Pt). Design Dt15.2 has an additional 10-nt overhang next to the cholesterol group, which is expected to reduce aggregation (41).

Membrane-binding experiments were performed using the gel shift assay (Figure 5B-i and Supplementary Figure S18). Of the seven designs tested, the lowest percentage of bound tiles was observed for Dt1.4 at 48 ± 27%. The maximum percentage of bound tiles was observed for Dt15.2 at 89 ± 9%. Percentage of bound tiles for Dt6.1, Dt8.1, Pt8.1, Pt8.5 and Pt13.2 was 50 ± 15%, 62 ± 20%, 67 ± 23%, 80 ± 23% and 86 ± 15%, respectively. The control with no cholesterol had 40 ± 22% tiles bound to the membrane in this experiment. For microscopy, only three designs were selected: Dt1.4, Pt8.5 and Dt15.2. The C_R values of 1.07 ± 0.05, 1.15 ± 0.04 and 1.24 ± 0.04 were obtained for Dt1.4, Pt8.5 and Dt15.2, respectively (Figure 5B-ii). The percentage of tiles bound in the presence and absence of Cy5 fluorophores was compared, and no significant difference was observed (Supplementary Figure S19).

Effect of toehold position on strand displacement of cholesterol–DNA from DNA origami tiles

The effect of toehold position on releasing DNA tile binding to SUVs by strand displacement was then investigated for the 4C-LS configuration. A 10-nt toehold was used for strand displacement of the tile from SUVs, to facilitate displacement of the C2 cholesterol strand from the tile (Figure 1C). The toehold was designed to be either proximal (Pt) or distal (Dt) to the cholesterol modification.

Strand displacement was validated by folding DNA tiles with cholesterols and fluorophore (Cy5) such that the fluorophore attachment was dependent on the cholesterol attachment, similar to earlier experiments used to confirm cholesterol attachment (Figure 1B-iii and Supplementary Figure S12). The strand arrangement for each of the different designs and their toehold positions are shown in Figure 6A-i.

Toehold-mediated strand displacement of the cholesterol strand from the DNA tile was first validated without any binding to SUVs. When displacement strand D1 is added, it is expected to bind to the toehold on the handle H1 and initiate branch migration, displacing the C1–F1 complex. It was confirmed that strands C1–F1 were displaced from the tile on addition of D1, as indicated by decrease in Cy5 intensity of the DNA tile band in AGE (Figure 6A-iii and Supplementary Figure S20).

Displacement efficiency was compared at RT and 37°C for 30 min using 4 μM of strand D1 and 2.5 nM of tile. The percentage of Cy5 on the tile was determined from the gel as shown in Figure 6A-iii. The percentage of Cy5 on the tile for the no displacement control was taken as 100% and the percentages for the displacement samples were calculated relative to this. Greater displacement was observed for designs with the toehold distal to the cholesterol groups (Figure 6A-iii and Supplementary Figure S20). For the tested temperatures, we observed no significant change in the displacement of the designs with distal toeholds, which were all highly efficient, decreasing from 100% to <3% for all conditions tested. In contrast, displacement efficiency of designs with toehold proximal to the cholesterol groups showed temperature dependence. Only partial displacement was observed at RT (decrease from 100% to 34–39%), with improved displacement at 37°C (decrease from 100% to 0–9%).

Effect of toehold position on strand displacement of DNA tiles from liposomes

Strand displacement of lipid-bound DNA tiles was then tested. For these experiments, cholesterols were attached to the tile (Figure 1B-i) independently of the fluorophores (Figure 1B-ii). The effect of strand displacement of the cholesterol from the tile was compared before (pre-displaced) and after (displaced) incubation with liposomes.

A subset of designs previously tested for lipid binding (Figure 5B) and strand displacement in lipid-free conditions (Figure 6A-iii) was selected, consisting of designs Dt1.4, Dt 15.2 and Pt8.5. Previously, Dt1.4 had shown poor membrane binding but efficient strand displacement in lipid-free conditions. Dt15.2 had both high membrane binding and efficient strand displacement. Pt8.5 had high membrane binding but inefficient strand displacement at RT.

The percentage of lipid-bound tiles for each design was determined by gel analysis for each experimental condition (Figure 6B and Supplementary Figure S21). The results show Dt1.4 had poor initial membrane binding (32%), which made it difficult to determine whether there was a change in binding after strand displacement (38%, displaced; 33%, pre-displaced). Dt15.2 was observed to have both high initial membrane binding (86%) and a decrease in binding on strand displacement indicating successful dis-

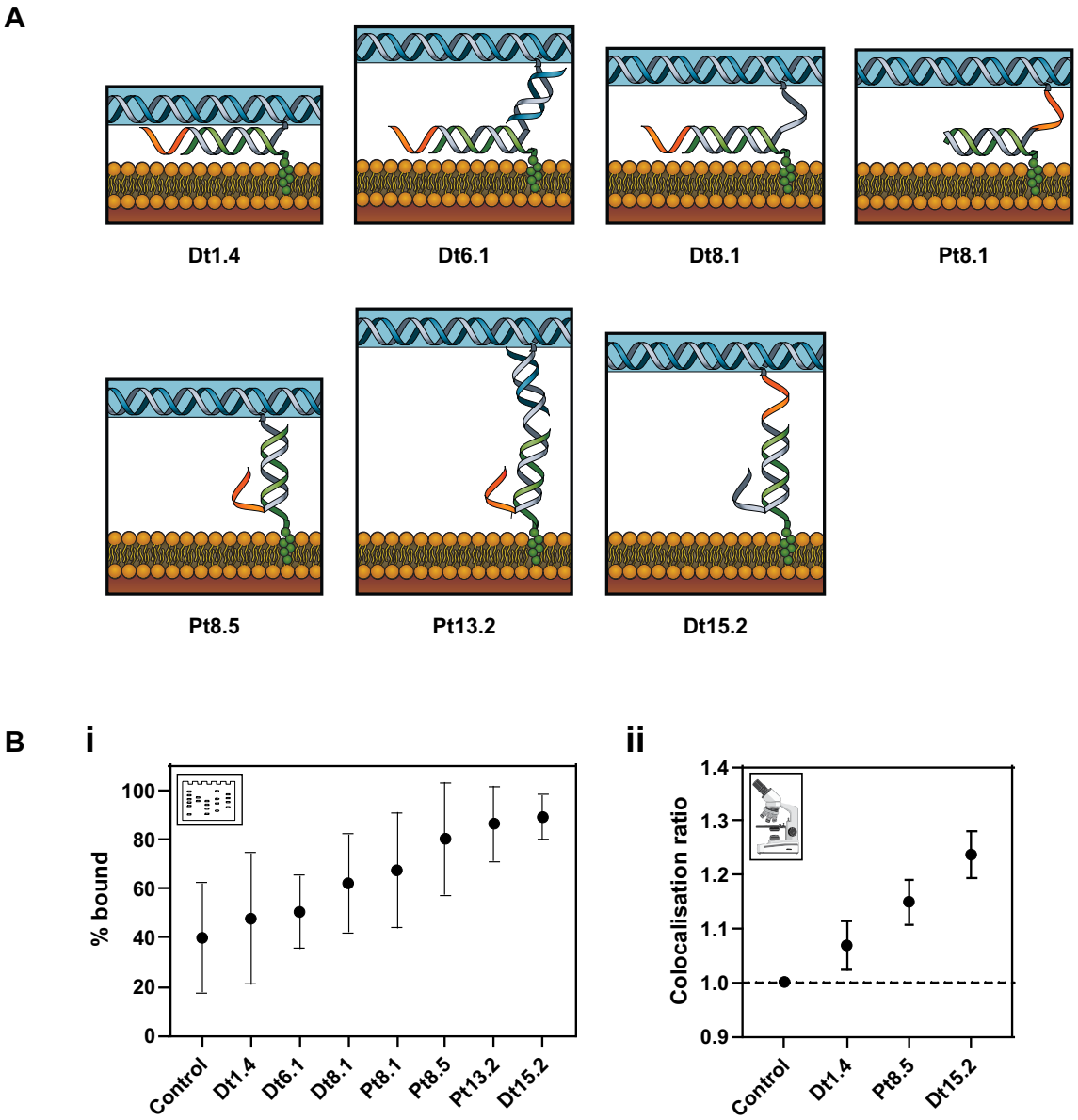

Figure 5. Effect of spacing and linker length between cholesterol and DNA origami tile on binding to liposomes. **(A)** Schematics for the different designs for cholesterol attachment to the tile and its membrane binding. **(B)** The effect of spacing between cholesterol and tile on the membrane binding. **(i)** Percentage bound obtained from gel analysis. **(ii)** Colocalization ratios from microscopy.

placement (39%, displaced; 36%, pre-displaced). Pt8.5 had moderate initial membrane binding (61%) and successful strand displacement (18%, displaced; 15%, pre-displaced). Comparing pre-displaced and displaced values, for all samples no significant effect was observed on changing the order of lipid binding and displacement. Hypothesized interactions of Dt1.4, Dt15.2 and Pt8.5 for both the bound and unbound tiles are proposed in Supplementary Figure S23.

DISCUSSION

Our comparison of the lipid-binding yield of simple DNA motifs (ssDNA, dsDNA, dsDNA-6nt) and large DNA origami tiles (7249 bp) modified with cholesterol defines a range of experimental conditions for which binding yield is independent of external buffer and lipid composition. Conveniently, we found that within this range, conditions can be selected based on the requirements of the DNA nanostructures or other system components.

DNA origami buffers are broadly compatible with liposome binding. DNA origami nanostructures often require specific ionic buffer conditions. Divalent cations such as Mg^{2+} stabilize DNA duplexes during nanostructure folding (72) and increase stability by inhibiting the electrostatic repulsion between DNA strands (54,67). Some DNA nanostructures are designed to change shape in response to changes in ion concentration and pH, acting as sensors (18). While changes in external buffer can cause changes in liposome membrane density and diffusivity (56,57), within the ranges tested here, addition of Na^{+} (0–200 mM) and

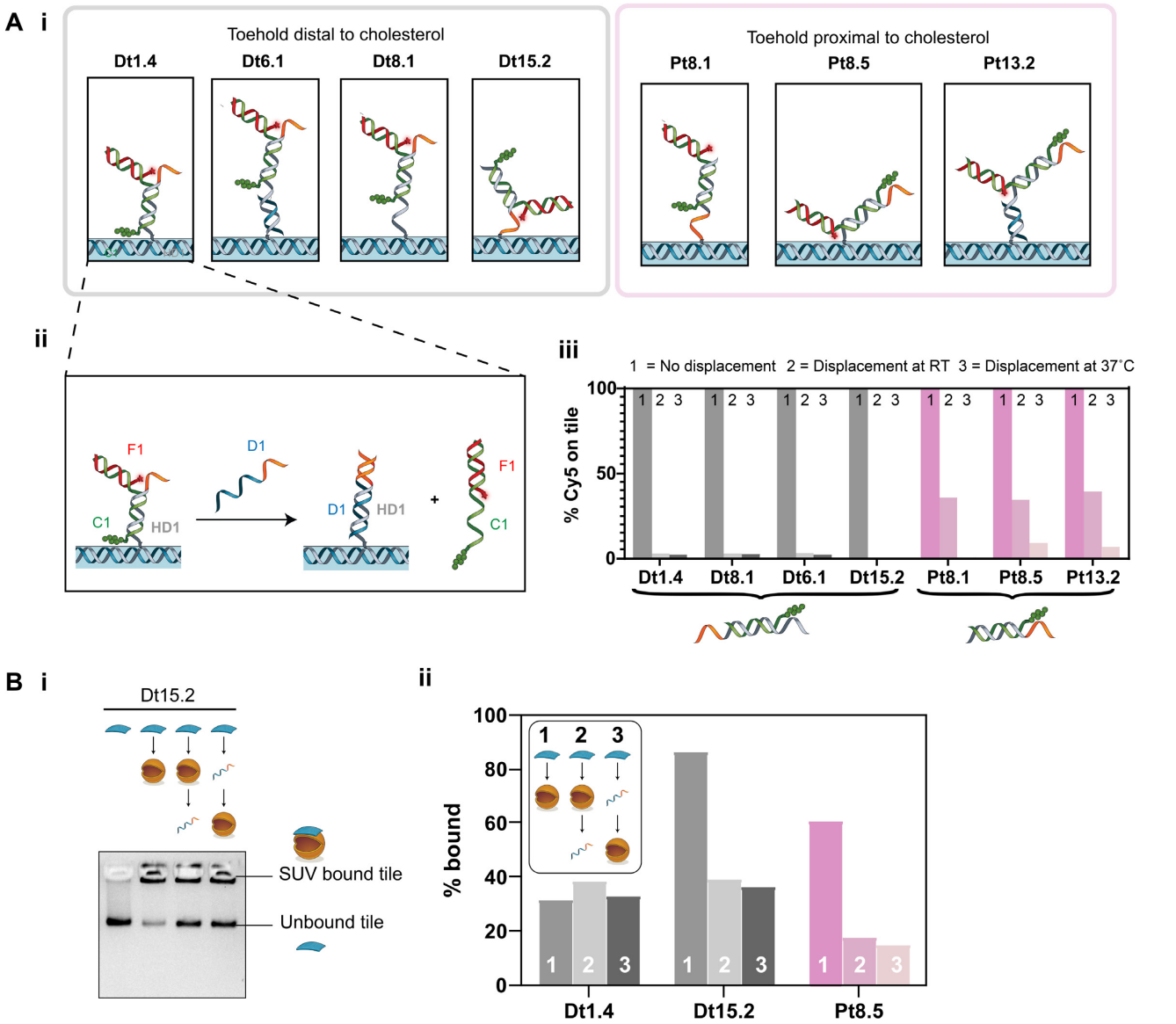

Figure 6. Effect of toehold position on strand displacement release of DNA tiles from liposomes. **(A) (i)** Schematics for the different designs for cholesterol attachment to the tile. **(ii)** Example strand displacement mechanism resulting in the detachment of the Cy5-labelled strand from the tile, shown here for design Dt1.4. **(iii)** Bar chart showing the percentage of Cy5 attached to the tile under different displacement conditions. In the control, no displacement strand is added; RT and 37°C represent displacement at RT and 37°C, respectively. **(B)** Strand displacement of membrane-bound tiles. **(i)** Gel image for Dt15.2. **(ii)** Percentage of tiles bound to the SUVs tabulated from the gel analysis. Designs with toeholds distal from the cholesterol groups are shown in shades of grey. Designs with toeholds proximal to the cholesterol groups are shown in shades of pink.

Mg^{2+} (0–40 mM) resulted in only a small decrease in DNA–lipid bindings, and no increase in non-specific binding of unmodified DNA was observed for any ionic condition.

Both DOPE/DOPC and DPhPC lipid mixtures were found to work well for lipid binding of DNA strands. DNA is highly negatively charged, while these liposomes are zwitterionic. Liposomes with DOPE would be expected to be positively charged below pH 3.5 and negatively charged above pH 8, while those with DPhPC would be expected to be neutral in this pH range and only become charged at a very low pH (e.g. pH 2) (73). We observed no change in lipid-binding yield or non-specific binding across the pH range 4–10 for both DPhPC or DOPE/DOPC liposomes, which suggests lipid ionization does not play a significant role in these conditions. However, we found that cholesterol-mediated lipid binding of DNA strands was completely inhibited in acidic conditions (pH 2). Hydronium ions (H_3O^+) are known to promote lipid–lipid binding interactions within a bilayer (74) and affect the behaviour of water molecules at the membrane–water interface (57). This could potentially lead to the inhibited binding that was observed in strongly acidic conditions (74).

Interestingly, we found that increasing the cholesterol content of lipid mixtures above 20% increased the binding of DNA strands to DOPE/DOPC liposomes but slightly decreased binding to DPhPC liposomes. Cholesterol in-

duces dense packing of phospholipids, reducing liposome permeability and increasing stability (75). Cholesterol also stabilizes the structure of some membrane proteins and promotes highly curved membrane intermediates during fusion (76). Branched-chain lipids like DPhPC occupy a greater area per molecule within a bilayer compared to linear-chain lipids such as DOPE and DOPC (77), and DPhPC has a lower cholesterol saturation limit than DOPE (78). Thus, the increased lipid binding of DNA strands that we observed with increasing cholesterol on DOPE/DOPC liposomes could be due to increased stability of the DNA-conjugated cholesterol in the membrane. The lower cholesterol saturation limit of DPhPC could explain why no further increase in lipid–DNA binding was observed above 20% cholesterol on DPhPC liposomes.

For small DNA motifs, dsDNA bound more efficiently to liposomes than ssDNA, and the addition of a 6-nt ssDNA overhang had minimal effect. Membrane-bound ssDNA has been observed to lie close to the surface of lipid bilayer membranes in fluorescence studies (79), while dsDNA remains in a stable position protruding normal to the membrane surface (80). Thus, the orientation difference of dsDNA compared to ssDNA may result in improved binding. The addition of a 6-nt overhang on cholesterol-tagged dsDNA strands has been proposed to assist nanostructure assembly by inhibiting strand aggregation (41). Inclusion of a 6-nt overhang next to the cholesterol group resulted in no significant decrease in binding for DOPE/DOPC liposomes, and but a significant, but small ($\Delta C_R = 0.10 \pm 0.46$) decrease in binding with the added overhang for DPhPC liposomes. This suggests that there is no large penalty from routine incorporation of overhangs on membrane-targeting nanostructures, but possible effects arising from other lipid compositions may need to be considered.

Upon studying the membrane binding of DNA strands, we next evaluated the membrane-binding behaviour of our DNA origami tile. We measured the number of cholesterols present on our DNA origami tile using fluorescence labelling and observed a non-linear increase in fluorescence as the number of cholesterols was increased. This non-linear increase in fluorescence could possibly be due to non-linear range of detection provided by the gel analysis (81) or self-quenching of the Cy5 fluorophores in close proximity on the tile (82,83), or from incomplete occupation of the H1 handles by cholesterol strands (84). Assuming incomplete occupation and linear fluorescence intensity per handle for low numbers (n = 0–4), we are able to estimate a lower bound for the actual cholesterol number in the $n = 16$ sample. Linear regression across zero to four handles estimates that our occupancy is 69% (for 16 cholesterols, our occupancy was 11 cholesterols with [7, 21] at 95% CI). This closely matches previous reports for mean staple occupancy of DNA origami tiles, which was measured as 72% for the same 10× staple excess folding conditions (84).

The number of cholesterol groups on a DNA origami tile had a large effect on binding yield. Adding a large number of hydrophobic groups has been shown to be necessary for overcoming the energy penalty associated with pore formation (9), and beneficial for maintaining stable insertion of a transmembrane nanopore (15). However, a large number of cholesterol groups may inhibit the membrane-binding function of cholesterol-tagged DNA nanostructures by inducing aggregation (41) or structural deformities (37). We found in our gel electrophoresis measurements that a global optimum for membrane binding occurred when there were $n = 4$ cholesterols. However, this was dependent on which assay was used: an optimum number of cholesterols of 8 was observed with the gel shift assay and an optimum number of 4 was observed with the microscopy.

We suggest that our observation of an optimal cholesterol number in these experiments is due to intra-tile and inter-tile transient binding of cholesterols. List *et al.* (37) showed that hydrophobic interactions between a large number of cholesterols (i.e. 35 cholesterols) on the DNA tile can result in the folding of the tile. Here, we did not observe deformation or aggregation of the tile on folding with higher cholesterol numbers (Supplementary Figures S12 and S13). However, it is possible that transient hydrophobic interactions occur between the cholesterol groups, which are not detected by gel or TEM. This would have the effect of decreasing the availability of cholesterols for binding to liposomes, and explain the observed decrease in membrane binding with increasing cholesterol number.

The difference in optimal cholesterol number obtained from the gel shift assay and the microscopy is likely due to the different tile purification methods used. For the gel shift assay, the tiles were gel purified. For microscopy, the tiles were purified by PEG precipitation to achieve higher concentrations of tile. PEG precipitation results in more aggregation compared to gel purification (Supplementary Figure S22). Higher aggregation results in more interaction between the tiles, and, in turn, is expected to decrease membrane binding.

We found that positioning cholesterols along the edge of tile resulted in more binding compared to cholesterols positioned at the centre of the tile, consistent with a previous study (30). We also found that the membrane binding of tiles increases as the spacing between the cholesterols and the tile increases. These trends are likely due to greater accessibility of the cholesterols at larger distances from the tile, and located at the edges of the tiles. The tile is flexible (40) and can fold, and the centre of the tile is more likely to be hidden compared to the edges. This may limit the accessibility of the cholesterols positioned at the centre and result in decreased membrane binding.

For all the results above, some non-specific binding was observed with the control tile (no cholesterol) in the gel shift assay. However, the amount of non-specific binding varied from gel to gel, and was found to vary between preparations of SUVs. Percentages of no-cholesterol tiles bound to the SUVs ranged from 15% to 60% across all the gels run in all different experiments. To control for this, our samples were always compared within gels, not between gels. Generally, microscopy experiments had smaller error ranges, while gel assays had larger errors but were higher throughput and useful for comparing large numbers of conditions.

We found that toehold-mediated strand displacement could be used to remove cholesterol-modified strands from the DNA tile with high efficiency, but that displacement efficiency decreased if the cholesterol was positioned directly adjacent to the toehold. This is likely due to the interaction of the toehold with the cholesterol group when it is

in proximity. Previous work by Ohmann *et al.* showed that an overhang placed next to a cholesterol can interact with it to reduce aggregation (41). An increase in temperature from RT to 37°C increased the displacement efficiency of these proximal designs to a similar value to designs where the cholesterol was located distal to the toehold.

Toehold-mediated strand displacement was shown to remove DNA tiles from liposomes, by separating the tile from the cholesterol strand. In this case, the cholesterol-modified DNA strand is expected to remain docked to the liposome. For cholesterol displacement of tiles already bound to liposomes, displacement was efficient for cholesterols positioned both proximal and distal to the toehold. This is in contrast to strand displacement in the absence of liposomes, where proximal toeholds had reduced efficiency. When the tile is bound to the liposome, we expect the cholesterol to have inserted into the bilayer. This may result in less interaction between cholesterol and toehold, making a more accessible toehold, facilitating more efficient strand displacement (Supplementary Figure S23). We expected to see reduced displacement efficacy for designs with shorter linkers (e.g. Dt1.4 compared to Dt15.2 and Pt8.5), because tight binding of the tile to the liposome might sterically hinder strand displacement. However, results here were dominated by the strong effect of linker length on initial binding yield. The short linker design had very low initial yield, comparable to non-specific binding, and so it was not possible to detect whether there was a decrease in strand displacement with the gel shift technique.

CONCLUSION

In this work, we tested different lipid species and DNA configurations to screen for optimal conditions to promote DNA–lipid binding. Our results suggest that lipid type, pH and DNA configuration are the most important parameters to consider when optimizing for the binding of DNA strands to liposomes, whereas mono- and divalent salt concentrations play a minor role.

Our results have shown that the membrane binding of DNA nanostructures to liposomes can be optimized by changing the cholesterol number, cholesterol configuration and cholesterol distance from the DNA nanostructure. We found that the optimal number of cholesterols for membrane binding of a 2D DNA origami tile is between 4 and 8, and that membrane binding is more favourable when cholesterol groups are placed at the edge of the tile compared to the centre of the tile. A larger linker length between the tiles and the cholesterol also results in greater membrane binding.

We demonstrated reversible membrane binding of the DNA nanostructures onto liposomes using toehold-mediated strand displacement. The efficiency of strand displacement is reduced if the toehold is adjacent to the cholesterol in unbound DNA nanostructures, but not for lipid-bound DNA nanostructures.

Future work could extend the findings from this work to more complex 3D DNA nanostructures with greater functionality. There is a general trade-off between increasing the lipid binding yield and decreasing aggregation. The flexibility of the 2D tile plays a role in aggregation, and so the greater rigidity of 3D DNA origami nanostructures may be an advantage. We anticipate our findings will provide guidelines for the design of more complex membrane-binding DNA nanostructures with broad applications in nanomedicine, nanotechnology and nucleic acid research.

SUPPLEMENTARY DATA

Supplementary Data are available at NAR Online.

ACKNOWLEDGEMENTS

The authors thank Dr. Jonathan Berengut for designing the liposome and tile schematic, and for helpful discussion. The authors also thank Minh Tri Luu for conducting RELION averaging of tiles, and for helpful discussion. The light microscopy imaging components of this study were carried out using instruments situated in, and maintained by, the Katharina Gaus – Light Microscopy Facility (KG-LMF) at UNSW.

FUNDING

Australian Research Council [DE180101635, DP210101892]; Commonwealth Scientific and Industrial Research Organisation; Westpac Bicentennial Foundation; The Medical Advances Without Animals Trust.
Conflict of interest statement. None declared.

REFERENCES

1. Seeman,N.C. and Sleiman,H.F. (2018) DNA nanotechnology. *Nat. Rev. Mater.*, **3**, 17068.
2. Seeman,N.C. (1982) Nucleic acid junctions and lattices. *J. Theor. Biol.*, **99**, 237–247.
3. Pinheiro,A.V., Han,D., Shih,W.M. and Yan,H. (2011) Challenges and opportunities for structural DNA nanotechnology. *Nat. Nanotechnol.*, **6**, 763–772.
4. Wang,P., Meyer,T.A., Pan,V., Dutta,P.K. and Ke,Y. (2017) The beauty and utility of DNA origami. *Chem*, **2**, 359–382.
5. Ding,B., Deng,Z., Yan,H., Cabrini,S., Zuckermann,R.N. and Bokor,J. (2010) Gold nanoparticle self-similar chain structure organized by DNA origami. *J. Am. Chem. Soc.*, **132**, 3248–3249.
6. Meyer,T.A., Zhang,C., Bao,G. and Ke,Y. (2020) Programmable assembly of iron oxide nanoparticles using DNA origami. *Nano Lett.*, **20**, 2799–2805.
7. Numajiri,K., Kimura,M., Kuzuya,A. and Komiyama,M. (2010) Stepwise and reversible nanopatterning of proteins on a DNA origami scaffold. *Chem. Commun.*, **46**, 5127–5129.
8. Ketterer,P., Ananth,A.N., Trip,D.S.L., Mishra,A., Bertosin,E., Ganji,M., van der Torre,J., Onck,P., Dietz,H. and Dekker,C. (2018) DNA origami scaffold for studying intrinsically disordered proteins of the nuclear pore complex. *Nat. Commun.*, **9**, 902.
9. Langecker,M., Arnaut,V., Martin,T.G., List,J., Renner,S., Mayer,M., Dietz,H. and Simmel,F.C. (2012) Synthetic lipid membrane channels formed by designed DNA nanostructures. *Science*, **338**, 932–936.
10. Burns,J.R., Göpfrich,K., Wood,J.W., Thacker,V.V., Stulz,E., Keyser,U.F. and Howorka,S. (2013) Lipid-bilayer-spanning DNA nanopores with a bifunctional porphyrin anchor. *Angew. Chem. Int. Ed.*, **52**, 12069–12072.
11. Kuzyk,A., Schreiber,R., Fan,Z., Pardatscher,G., Roller,E.-M., Högele,A., Simmel,F.C., Govorov,A.O. and Liedl,T. (2012) DNA-based self-assembly of chiral plasmonic nanostructures with tailored optical response. *Nature*, **483**, 311–314.
12. Liu,W., Halverson,J., Tian,Y., Tkachenko,A.V. and Gang,O. (2016) Self-organized architectures from assorted DNA-framed nanoparticles. *Nat. Chem*, **8**, 867–873.

13. Kuzuya,A., Sakai,Y., Yamazaki,T., Xu,Y. and Komiyama,M. (2011) Nanomechanical DNA origami 'single-molecule beacons' directly imaged by atomic force microscopy. *Nat. Commun.*, **2**, 1–8.
14. Kuzuya,A., Watanabe,R., Yamanaka,Y., Tamaki,T., Kaino,M. and Ohya,Y. (2014) Nanomechanical DNA origami pH sensors. *Sensors*, **14**, 19329–19335.
15. Krishnan,S., Ziegler,D., Arnaut,V., Martin,T.G., Kapsner,K., Henneberg,K., Bausch,A.R., Dietz,H. and Simmel,F.C. (2016) Molecular transport through large-diameter DNA nanopores. *Nat. Commun.*, **7**, 12787.
16. Zhang,D.Y. and Winfree,E. (2009) Control of DNA strand displacement kinetics using toehold exchange. *J. Am. Chem. Soc.*, **131**, 17303–17314.
17. Qian,L. and Winfree,E. (2011) Scaling up digital circuit computation with DNA strand displacement cascades. *Science*, **332**, 1196–1201.
18. Daljit Singh,J.K., Luu,M.T., Abbas,A. and Wickham,S.F.J. (2018) Switchable DNA-origami nanostructures that respond to their environment and their applications. *Biophys. Rev.*, **10**, 1283–1293.
19. Göpfrich,K., Zettl,T., Meijering,A.E.C., Hernández-Ainsa,S., Kocabey,S., Liedl,T. and Keyser,U.F. (2015) DNA-tile structures induce ionic currents through lipid membranes. *Nano Lett.*, **15**, 3134–3138.
20. Burns,J.R., Seifert,A., Fertig,N. and Howorka,S. (2016) A biomimetic DNA-based channel for the ligand-controlled transport of charged molecular cargo across a biological membrane. *Nat. Nanotechnol.*, **11**, 152.
21. Iric,K., Subramanian,M., Oertel,J., Agarwal,N.P., Matthies,M., Periole,X., Sakmar,T.P., Huber,T., Fahmy,K. and Schmidt,T.L. (2018) DNA-encircled lipid bilayers. *Nanoscale*, **10**, 18463–18467.
22. Rodríguez-Pulido,A., Kondrachuk,A.I., Prusty,D.K., Gao,J., Loi,M.A. and Herrmann,A. (2012) Light-triggered sequence-specific cargo release from DNA block copolymer-lipid vesicles. *Angew. Chem. Int. Ed. Engl.*, **52**, 1008–1012.
23. Göpfrich,K., Li,C.-Y., Mames,I., Bhamidimarri,S.P., Ricci,M., Yoo,J., Mames,A., Ohmann,A., Winterhalter,M., Stulz,E. *et al.* (2016) Ion channels made from a single membrane-spanning DNA duplex. *Nano Lett.*, **16**, 4665–4669.
24. Bell,N.A. and Keyser,U.F. (2014) Nanopores formed by DNA origami: a review. *FEBS Lett.*, **588**, 3564–3570.
25. Akbari,E., Mollica,M.Y., Lucas,C.R., Bushman,S.M., Patton,R.A., Shahhosseini,M., Song,J.W. and Castro,C.E. (2017) Engineering cell surface function with DNA origami. *Adv. Mater.*, **29**, 1703632.
26. Franquelim,H.G., Khmelinskaia,A., Sobczak,J.-P., Dietz,H. and Schwille,P. (2018) Membrane sculpting by curved DNA origami scaffolds. *Nat. Commun.*, **9**, 811.
27. Grome,M.W., Zhang,Z., Pincet,F. and Lin,C. (2018) Vesicle tubulation with self-assembling DNA nanosprings. *Angew. Chem. Int. Ed.*, **57**, 5330–5334.
28. Diederichs,T., Pugh,G., Dorey,A., Xing,Y., Burns,J.R., Nguyen,Q.H., Tornow,M., Tampé,R. and Howorka,S. (2019) Synthetic protein-conductive membrane nanopores built with DNA. *Nat. Commun.*, **10**, 1–11.
29. Mendoza,O., Calmet,P., Alves,I., Lecomte,S., Raoux,M., Cullin,C. and Elezgaray,J. (2017) A tensegrity driven DNA nanopore. *Nanoscale*, **9**, 9762–9769.
30. Khmelinskaia,A., Franquelim,H.G., Petrov,E.P. and Schwille,P. (2016) Effect of anchor positioning on binding and diffusion of elongated 3D DNA nanostructures on lipid membranes. *J. Phys. D Appl. Phys.*, **49**, 194001.
31. Khmelinskaia,A., Mücksch,J., Petrov,E.P., Franquelim,H.G. and Schwille,P. (2018) Control of membrane binding and diffusion of cholesteryl-modified DNA origami nanostructures by DNA spacers. *Langmuir*, **34**, 14921–14931.
32. Chidchob,P., Offenbartl-Stiegert,D., McCarthy,D., Luo,X., Li,J., Howorka,S. and Sleiman,H.F. (2019) Spatial presentation of cholesterol units on a DNA cube as a determinant of membrane protein-mimicking functions. *J. Am. Chem. Soc.*, **141**, 1100–1108.
33. Rothemund,P.W.K. (2006) Folding DNA to create nanoscale shapes and patterns. *Nature*, **440**, 297–302.
34. Liu,Y., Wijesekara,P., Kumar,S., Wang,W., Ren,X. and Taylor,R.E. (2021) The effects of overhang placement and multivalency on cell labeling by DNA origami. *Nanoscale*, **13**, 6819–6828.
35. Thomsen,R.P., Malle,M.G., Okholm,A.H., Krishnan,S., Bohr,S.S., Sørensen,R.S., Ries,O., Vogel,S., Simmel,F.C., Hatzakis,N.S. *et al.* (2019) A large size-selective DNA nanopore with sensing applications. *Nat. Commun.*, **10**, 5655.
36. Göpfrich,K., Li,C.-Y., Ricci,M., Bhamidimarri,S.P., Yoo,J., Gyenes,B., Ohmann,A., Winterhalter,M., Aksimentiev,A. and Keyser,U.F. (2016) Large-conductance transmembrane porin made from DNA origami. *ACS Nano*, **10**, 8207–8214.
37. List,J., Weber,M. and Simmel,F.C. (2014) Hydrophobic actuation of a DNA origami bilayer structure. *Angew. Chem. Int. Ed.*, **53**, 4236–4239.
38. Bastings,M.M.C., Anastassacos,F.M., Ponnuswamy,N., Leifer,F.G., Cuneo,G., Lin,C., Ingber,D.E., Ryu,J.H. and Shih,W.M. (2018) Modulation of the cellular uptake of DNA origami through control over mass and shape. *Nano Lett.*, **18**, 3557–3564.
39. Wang,P., Rahman,M.A., Zhao,Z., Weiss,K., Zhang,C., Chen,Z., Hurwitz,S.J., Chen,Z.G., Shin,D.M. and Ke,Y. (2018) Visualization of the cellular uptake and trafficking of DNA origami nanostructures in cancer cells. *J. Am. Chem. Soc.*, **140**, 2478–2484.
40. Baker,M.A.B., Tuckwell,A.J., Berengut,J.F., Bath,J., Benn,F., Duff,A.P., Whitten,A.E., Dunn,K.E., Hynson,R.M., Turberfield,A.J. *et al.* (2018) Dimensions and global twist of single-layer DNA origami measured by small-angle X-ray scattering. *ACS Nano*, **12**, 5791–5799.
41. Ohmann,A., Göpfrich,K., Joshi,H., Thompson,R.F., Sobota,D., Ranson,N.A., Aksimentiev,A. and Keyser,U.F. (2019) Controlling aggregation of cholesterol-modified DNA nanostructures. *Nucleic Acids Res.*, **47**, 11441–11451.
42. Simanshu,D.K., Nissley,D.V. and McCormick,F. (2017) RAS proteins and their regulators in human disease. *Cell*, **170**, 17–33.
43. Stoeckelhuber,M., Noegel,A.A., Eckerskorn,C., Kohler,J., Rieger,D. and Schleicher,M. (1996) Structure/function studies on the pH-dependent actin-binding protein hisactophilin in *Dictyostelium* mutants. *J. Cell Sci.*, **109**, 1825–1835.
44. Parsons,S.J. and Parsons,J.T. (2004) Src family kinases, key regulators of signal transduction. *Oncogene*, **23**, 7906–7909.
45. Burn, P. (1988) Amphitropic proteins: a new class of membrane proteins. *Trends Biochem. Sci.*, **13**, 79–83.
46. Johnson,J.E. and Cornell,R.B. (1999) Amphitropic proteins: regulation by reversible membrane interactions. *Mol. Membr. Biol.*, **16**, 217–235.
47. Conway,J.W., Madwar,C., Edwardson,T.G., McLaughlin,C.K., Fahkoury,J., Lennox,R.B. and Sleiman,H.F. (2014) Dynamic behavior of DNA cages anchored on spherically supported lipid bilayers. *J. Am. Chem. Soc.*, **136**, 12987–12997.
48. Morzy,D., Rubio-Sánchez,R., Joshi,H., Aksimentiev,A., Di Michele,L. and Keyser,U.F. (2021) Cations regulate membrane attachment and functionality of DNA nanostructures. *J. Am. Chem. Soc.*, **143**, 7358–7367.
49. Yang,Y., Wang,J., Shigematsu,H., Xu,W., Shih,W.M., Rothman,J.E. and Lin,C. (2016) Self-assembly of size-controlled liposomes on DNA nanotemplates. *Nat. Chem.*, **8**, 476.
50. Yang,Y., Wu,Z., Wang,L., Zhou,K., Xia,K., Xiong,Q., Liu,L., Zhang,Z., Chapman,E.R., Xiong,Y. *et al.* (2021) Sorting sub-150-nm liposomes of distinct sizes by DNA-brick-assisted centrifugation. *Nat. Chem.*, **13**, 335–342.
51. Haley,N.E.C., Ouldridge,T.E., Mullor Ruiz,I., Geraldini,A., Louis,A.A., Bath,J. and Turberfield,A.J. (2020) Design of hidden thermodynamic driving for non-equilibrium systems via mismatch elimination during DNA strand displacement. *Nat. Commun.*, **11**, 2562.
52. Machinek,R.R.F., Ouldridge,T.E., Haley,N.E.C., Bath,J. and Turberfield,A.J. (2014) Programmable energy landscapes for kinetic control of DNA strand displacement. *Nat. Commun.*, **5**, 5324.
53. Jahnke,K., Grubmüller,H., Igaev,M. and Göpfrich,K. (2021) Choice of fluorophore affects dynamic DNA nanostructures. *Nucleic Acids Res.*, **49**, 4186–4195.
54. Kielar,C., Xin,Y., Shen,B., Kostiainen,M.A., Grundmeier,G., Linko,V. and Keller,A. (2018) On the stability of DNA origami nanostructures in low-magnesium buffers. *Angew. Chem. Int. Ed.*, **57**, 9470–9474.
55. Nakano,S., Fujimoto,M., Hara,H. and Sugimoto,N. (1999) Nucleic acid duplex stability: influence of base composition on cation effects. *Nucleic Acids Res.*, **27**, 2957–2965.

56. Böckmann,R.A., Hac,A., Heimburg,T. and Grubmüller,H. (2003) Effect of sodium chloride on a lipid bilayer. *Biophys. J.*, **85**, 1647–1655.
57. Velikonja,A., Perutkova,Š., Gongadze,E., Kramar,P., Polak,A., Maček-Lebar,A. and Iglič,A. (2013) Monovalent ions and water dipoles in contact with dipolar zwitterionic lipid headgroups—theory and MD simulations. *Int. J. Mol. Sci.*, **14**, 2846–2861.
58. Arnott,P.M., Joshi,H., Aksimentiev,A. and Howorka,S. (2018) Dynamic interactions between lipid-tethered DNA and phospholipid membranes. *Langmuir*, **34**, 15084–15092.
59. Jones,S.F., Joshi,H., Terry,S.J., Burns,J.R., Aksimentiev,A., Eggert,U.S. and Howorka,S. (2021) Hydrophobic interactions between DNA duplexes and synthetic and biological membranes. *J. Am. Chem. Soc.*, **143**, 8305–8313.
60. Zadeh,J.N., Steenberg,C.D., Bois,J.S., Wolfe,B.R., Pierce,M.B., Khan,A.R., Dirks,R.M. and Pierce,N.A. (2011) NUPACK: analysis and design of nucleic acid systems. *J. Comput. Chem.*, **32**, 170–173.
61. Kreir,M., Farre,C., Beckler,M., George,M. and Fertig,N. (2008) Rapid screening of membrane protein activity: electrophysiological analysis of OmpF reconstituted in proteoliposomes. *Lab Chip*, **8**, 587–595.
62. Baker,M.A.B., Nieves,D.J., Hilzenrat,G., Berengut,J.F., Gaus,K. and Lee,L.K. (2019) Stoichiometric quantification of spatially dense assemblies with qPAINT. *Nanoscale*, **11**, 12460–12464.
63. Jungmann,R., Avendaño,M.S., Woehrstein,J.B., Dai,M., Shih,W.M. and Yin,P. (2014) Multiplexed 3D cellular super-resolution imaging with DNA-PAINT and Exchange-PAINT. *Nat. Methods*, **11**, 313–318.
64. Schindelin,J., Arganda-Carreras,I., Frise,E., Kaynig,V., Longair,M., Pietzsch,T., Preibisch,S., Rueden,C., Saalfeld,S. and Schmid,B. (2012) Fiji: an open-source platform for biological-image analysis. *Nat. Methods*, **9**, 676–682.
65. Dunn,K.W., Kamocka,M.M. and McDonald,J.H. (2011) A practical guide to evaluating colocalization in biological microscopy. *Am. J. Physiol. Cell Physiol.*, **300**, C723–C742.
66. Schnitzbauer,J., Strauss,M.T., Schlichthaerle,T., Schueder,F. and Jungmann,R. (2017) Super-resolution microscopy with DNA-PAINT. *Nat. Protoc.*, **12**, 1198–1228.
67. Douglas,S.M., Dietz,H., Liedl,T., Högberg,B., Graf,F. and Shih,W.M. (2009) Self-assembly of DNA into nanoscale three-dimensional shapes. *Nature*, **459**, 414–418.
68. Stahl,E., Martin,T.G., Praetorius,F. and Dietz,H. (2014) Facile and scalable preparation of pure and dense DNA origami solutions. *Angew. Chem. Int. Ed.*, **53**, 12735–12740.
69. Lanphere,C., Offenbartl-Stiegert,D., Dorey,A., Pugh,G., Georgiou,E., Xing,Y., Burns,J.R. and Howorka,S. (2021) Design, assembly, and characterization of membrane-spanning DNA nanopores. *Nat. Protoc.*, **16**, 86–130.
70. Scheres,S.H.W. (2012) RELION: implementation of a Bayesian approach to cryo-EM structure determination. *J. Struct. Biol.*, **180**, 519–530.
71. Johnson-Buck,A., Jiang,S., Yan,H. and Walter,N.G. (2014) DNA–cholesterol barges as programmable membrane-exploring agents. *ACS Nano*, **8**, 5641–5649.
72. Owczarzy,R., Moreira,B.G., You,Y., Behlke,M.A. and Walder,J.A. (2008) Predicting stability of DNA duplexes in solutions containing magnesium and monovalent cations. *Biochemistry*, **47**, 5336–5353.
73. Tsui,F.C., Ojcius,D.M. and Hubbell,W.L. (1986) The intrinsic pK_a values for phosphatidylserine and phosphatidylethanolamine in phosphatidylcholine host bilayers. *Biophys. J.*, **49**, 459.
74. Deplazes,E., Poger,D., Cornell,B. and Cranfield,C.G. (2018) The effect of hydronium ions on the structure of phospholipid membranes. *Phys. Chem. Chem. Phys.*, **20**, 357–366.
75. Róg,T., Pasenkiewicz-Gierula,M., Vattulainen,I. and Karttunen,M. (2009) Ordering effects of cholesterol and its analogues. *Biochim. Biophys. Acta Biomembr.*, **1788**, 97–121.
76. Yang,S.-T., Kreutzberger,A.J.B., Lee,J., Kiessling,V. and Tamm,L.K. (2016) The role of cholesterol in membrane fusion. *Chem. Phys. Lipids*, **199**, 136–143.
77. Tristram-Nagle,S., Kim,D.J., Akhunzada,N., Kučerka,N., Mathai,J.C., Katsaras,J., Zeidel,M. and Nagle,J.F. (2010) Structure and water permeability of fully hydrated diphytanoylPC. *Chem. Phys. Lipids*, **163**, 630–637.
78. Huang,J., Buboltz,J.T. and Feigenson,G.W. (1999) Maximum solubility of cholesterol in phosphatidylcholine and phosphatidylethanolamine bilayers. *Biochim. Biophys. Acta Biomembr.*, **1417**, 89–100.
79. Roy,R., Hohng,S. and Ha,T. (2008) A practical guide to single-molecule FRET. *Nat. Methods*, **5**, 507–516.
80. Ma,D., Xu,C., Hou,W., Zhao,C., Ma,J., Huang,X., Jia,Q., Ma,L., Diao,J. and Liu,C. (2019) Detecting single-molecule dynamics on lipid membranes with quenchers-in-a-liposome FRET. *Angew. Chem.*, **131**, 5633–5637.
81. Schröder,S., Zhang,H., Yeung,E.S., Jänsch,L., Zabel,C. and Wätzig,H. (2008) Quantitative gel electrophoresis: sources of variation. *J. Proteome Res.*, **7**, 1226–1234.
82. Berlier,J.E., Rothe,A., Buller,G., Bradford,J., Gray,D.R., Filanoski,B.J., Telford,W.G., Yue,S., Liu,J., Cheung,C.-Y. *et al.* (2003) Quantitative comparison of long-wavelength Alexa Fluor dyes to Cy dyes: fluorescence of the dyes and their bioconjugates. *J. Histochem. Cytochem.*, **51**, 1699–1712.
83. Hahn,C.D., Riener,C.K. and Gruber,H.J. (2001) Labeling of antibodies with Cy3-, Cy3.5-, Cy5-, and Cy5.5-monofunctional dyes at defined dye/protein ratios. *Single Mol.*, **2**, 149–149.
84. Strauss,M.T., Schueder,F., Haas,D., Nickels,P.C. and Jungmann,R. (2018) Quantifying absolute addressability in DNA origami with molecular resolution. *Nat. Commun.*, **9**, 1600.